Colloids and Surfaces A 558 (2018) 192–199

Contents lists available at ScienceDirect

Colloids and Surfaces A

journal homepage: www.elsevier.com/locate/colsurfa

Atomised spray plasma deposition of hierarchical superhydrophobic nanocomposite surfaces

I. Castaneda-Montes, A.W. Ritchie, J.P.S. Badyal*

Chemistry Department, Science Laboratories, Durham University, Durham DH1 3LE, England, UK

GRAPHICAL ABSTRACT

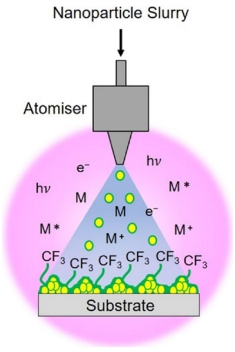

ARTICLE INFO

Keywords:
Bioinspired
Superhydrophobic
Nanocomposite
Atomised spray plasma deposition
Liquid repellency
Microindentation

ABSTRACT

Atomised spray plasma deposition (ASPD) using perfluorotributylamine–nanoparticle slurry mixtures yields superhydrophobic nanocomposite layers in a single solventless step. X-ray photoelectron and infrared spectroscopies indicate the formation of a poly(perfluorocarbon) host matrix containing nanoparticles. Electron microscopy shows the appearance of hierarchical surface roughness through the incorporation of nanoparticles. This gives rise to a synergistic effect combining low surface perfluoroalkyl groups and surface roughness leading to enhanced water and oil (hexadecane) contact angle values. Microindentation measurements show that the mechanical properties of the deposited liquid repellent nanocomposite layer are enhanced through the incorporation of methacryloyl functionalised silica, zinc oxide, or graphene nanoparticles.

1. Introduction

Liquid repellent surfaces have attracted significant interest for societal and industrial applications, including: self-cleaning [1], anti-icing [2], anti-fogging [3], building materials [4], electronic devices [5], antifouling [6], anti-corrosion [7], antibacterial [8], drag reduction [9], oil–water separation [10,11], and anti-thrombotic surfaces [12]. One approach for attaining hydrophobicity is inspired by the water repellency properties of the lotus leaf (*Nelumbo nucifera*)—which contains microscale surface bumps (papillose epidermal cells) covered by nanoscale epicuticular waxes [13]. This hierarchical roughness reduces the solid–liquid contact line by increasing the liquid–air contact line due to entrapped air pockets at the composite solid–liquid–air interface, thereby facilitating the movement of droplets along the plant leaf surface leading to self-cleaning [14].

A combination of such hierarchical roughness with low surface energy materials for the preparation of superhydrophobic surfaces has been reported in the past by fabrication methods such as:

* Corresponding author.
E-mail address: j.p.badyal@durham.ac.uk (J.P.S. Badyal).

https://doi.org/10.1016/j.colsurfa.2018.08.054
Received 27 June 2018; Received in revised form 24 August 2018; Accepted 24 August 2018
Available online 27 August 2018

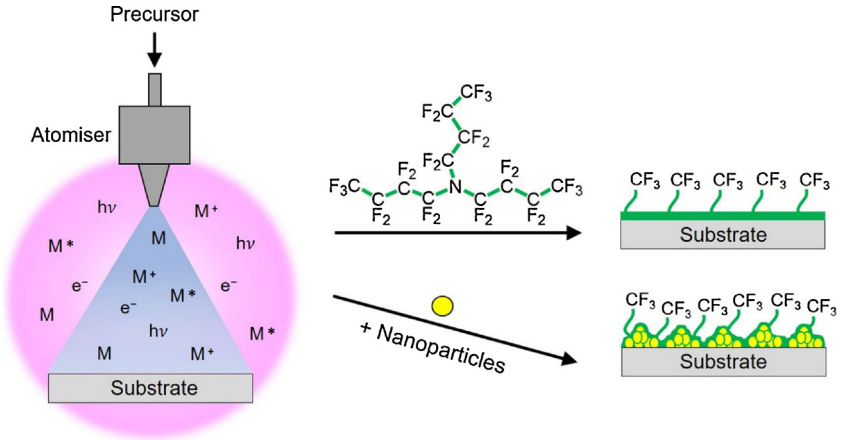

Scheme 1. Atomised spray plasma deposition (ASPD) of perfluorotributylamine–nanoparticle nanocomposite layer.

photopolymerisation [1], spray casting [15], electrodeposition [16], hydrothermal process [9], chemical vapour deposition [17], plasma polymerisation [18], sol-gel [19], electrowetting [20], layer-by-layer [21,22], dip coating [23], lithography [24], fluorination [25], and etching [26]. However, many of these techniques suffer from limitations, including: solvents [15,27], multi-step [17,19,28], lengthy [3], requiring high vapour pressure precursors [29], post-heat treatments [4], poor adhesion [30], etc.

In this article, we describe an approach which overcomes the aforementioned disadvantages. This comprises the single-step atomised spray plasma deposition (ASPD) of liquid repellent nanocomposite coatings using a low surface energy precursor–nanoparticle slurry (perfluorotributylamine mixed with methacryloyl functionalised silica, zinc oxide, or graphene nanoparticles), which yields hierarchical roughness and mechanical hardness, Scheme 1. The selection of a fluorocarbon precursor provides for both water and oil repellency, and the utilisation of a sub-atmospheric pressure plasma avoids the requirement for expensive carrier gases as well as providing the safe removal of volatile toxic low molecular by-product species [31].

2. Experimental

2.1. Atomised spray plasma deposition

Precursor materials used were perfluorotributylamine (+99.9%, Fluorinert FC-43, 3M Inc.), and a variety of nanoparticles: methacryloyl functionalised silica nanoparticles (12 nm primary particle size and 100–200 nm average aggregate size, Aerosil R711®, Evonik Industries AG); zinc oxide nanoparticles (< 100 nm particle size, Sigma-Aldrich Ltd.); and graphene nanoplatelets (2–10 nm thickness and < 2 µm particle diameter, Strem Chemicals UK Ltd.). Unfunctionalised silica nanoparticles display hydrophilic behaviour due to surface hydroxyl groups, and were found not to readily disperse in low surface tension liquids (e.g. perfluorotributylamine). Instead, methacryloyl functionalised SiO_2 nanoparticles (methacryloyl-SiO_2) were used due to their ease of dispersion in non-polar liquids [32]. For the case of perfluorotributylamine precursor mixed with methacryloyl functionalised silica and zinc oxide nanoparticles (ratio 1:1 w/w), 5% v/v of trifluoroacetic acid (+99%, Fluorochem Ltd.) was added to improve dispersion (carboxylic acid groups can interact with ZnO surfaces) [33,34]. Liquid monomer–nanoparticle mixtures were sonicated for 45–60 min to fully disperse the nanoparticles (Clifton ultrasonic bath, Nickel-Electro Ltd.), and then loaded into a sealable glass delivery tube. This precursor slurry mixture was then degassed using several freeze–pump–thaw cycles. Substrates used for coating were glass microscope slides (Academy Science Ltd.) and silicon (100) wafers (0.014–0.024 Ω cm resistivity, Silicon Valley Microelectronics Inc.). These were cleaned in three steps: ultrasonicated in a 1:1 v/v mixture of propan-2-ol (+99.5 wt %, Fisher Scientific Ltd.)/cyclohexane (+99.7%, Sigma-Aldrich Ltd.) for 5 min and air dried, followed by UV ozone cleaning (ProCleaner model UV.TC.EU.003, BioForce Nanosciences Inc.) for 10 min, and finally ultrasonicated in a 1:1 v/v solvent mixture of propan-2-ol/cyclohexane for 5 min followed by air drying before placement downstream in line-of-sight from the atomiser, Fig. 1.

Atomised spray plasma deposition was carried out in an electrodeless, cylindrical, T-shape glass reactor (volume 1117 cm^3, base pressure of 3×10^{-3} mbar, and a leak rate better than 2×10^{-9} mol s^{-1}) [35] enclosed in a Faraday cage. The chamber was pumped by a 30 L min^{-1} two-stage rotary pump (model E2M2, Edwards Vacuum Ltd.) attached to a liquid nitrogen cold trap, and the system pressure monitored by a thermocouple gauge. An L–C impedance matching network was used to minimise the standing wave ratio for power transmitted from a 13.56 MHz radio frequency (RF) power supply to a copper coil (4 mm diameter, 7 turns) located downstream from an atomiser (20 µm diameter median droplet size [36,37], model No. 8700-120, Sono-Tek Corp.), which was driven by a broadband ultrasonic generator (120 kHz, model No. 06-05108, Sono-Tek Corp.). Prior to each deposition, the chamber was scrubbed with detergent, rinsed with propan-2-ol and acetone (+99%, Fisher Scientific Ltd.), and oven dried. Next, a continuous wave air plasma was run at 0.2 mbar pressure and 50 W power for 30 min to remove any remaining trace contaminants from the chamber walls. Ambient temperature deposition was carried out using a 30 W continuous wave plasma in conjunction with atomisation of the solid–liquid slurry into the reaction chamber employing an optimised flow rate of $16 \pm 4 \times 10^{-4}$ mL s^{-1} (higher flow rates produce unstable films due to incomplete polymerisation). Upon plasma extinction, the atomiser was switched off and the system was evacuated to base pressure, followed by venting to atmosphere. The chemical stability of the deposited nanocomposite layers towards polar and non-

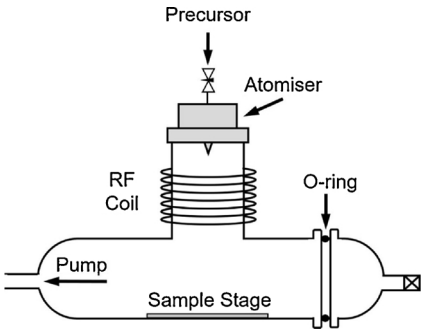

Fig. 1. Atomised spray plasma deposition (ASPD) chamber.

polar solvents was tested by rinsing the samples with a 1:1 v/v mixture of propan-2-ol/cyclohexane for 1 min and air dried. Control experiments showed that in the absence of plasma ignition, the atomiser deposited layers could be readily washed off with polar and non-polar solvents.

2.2. Contact angle analysis

Sessile drop static contact angle measurements were carried out at 20 °C using a video capture apparatus in combination with a motorised syringe (model VCA 2500XE, A.S.T. Products Inc.). 1.0 µL droplets of ultrahigh-purity water (B.S. 3978 grade 1) and hexadecane (99%, Sigma-Aldrich Ltd.) were employed as probe liquids for hydrophobicity and oleophobicity respectively. Advancing and receding contact angle values were determined by respectively increasing the dispensed 1.0 µL liquid drop volume by a further 1.0 µL, and then decreasing the liquid drop volume by 1.0 µL [38].

2.3. X-ray photoelectron spectroscopy

Deposited layers were analysed by X-ray photoelectron spectroscopy (XPS) using a VG ESCALAB II electron spectrometer equipped with a non-monochromated Mg Kα X-ray source (1253.6 eV) and a concentric hemispherical analyser. Photoemitted electrons were collected at a take-off angle of 20° from the substrate normal with electron detection in the constant analyser energy mode (CAE, pass energy = 20 eV) [39]. Experimentally determined instrument sensitivity (multiplication) factors were C(1s):N(1s):F(1s):O(1s):Si(2p):Zn (2p) equals 1.00:0.70:0.25:0.35:0.97:0.056 [39]. A linear background was subtracted from core level spectra and then fitted using Gaussian peak shapes with a constant full-width-half-maximum (FWHM) [40,41]. All binding energies are referenced to the Mg $K\alpha_{1,2}$ C(1s) $-\underline{C}F_2-$ peak at 291.2 eV binding energy [42,43].

2.4. Infrared spectroscopy

Fourier transform infrared (FTIR) analysis was carried out using an FTIR spectrometer (Spectrum One, Perkin Elmer Inc.) equipped with a liquid nitrogen cooled mercury cadmium telluride (MCT) detector. The spectra were averaged over 285 scans at a resolution of 4 cm^{-1} across the 450–4000 cm^{-1} range. Reflection–absorption infrared spectroscopy (RAIRS) of ASPD nanocomposite layer coated silicon wafers was performed using a variable angle reflection–absorption accessory (Specac Ltd.) fitted with mirrors aligned at an angle of 66° to the substrate normal. Attenuated–total–reflection (ATR) spectra of perfluorotributylamine, methacryloyl-SiO_2 nanoparticles, ZnO nanoparticles, and graphene nanoplatelets were obtained using a single reflection type II-a diamond brazed into tungsten carbide accessory (Golden Gate, Specac Ltd.).

2.5. Scanning electron microscopy

ASPD coated silicon wafers were mounted onto carbon disks supported by aluminium stubs, and then covered with a 5–10 nm evaporated gold layer (Polaron SEM Coating Unit, Quorum Technologies Ltd.). Surface morphology images were acquired on a scanning electron microscope (model Vega 3LMU, Tescan Orsay Holding, a.s.) operating in secondary electron detection mode at an accelerating voltage of 8 kV, and a working distance of 8–10 mm.

2.6. Microindentation

Vickers hardness (HV) values were measured using a micro Vickers hardness tester (model MVK-H2, Mitutoyo Inc.) and then converted into GPa. A standard Vickers indenter tip was employed with applied loads of 98, 245, 490, and 980 mN (international standard test ASTM E384-11e1) [44]. The tip load was applied for 10 s, at an indentation speed of 3 µm s^{-1} and then unloaded over a period of 10 s. At least 5 different sampling points across the surface were analysed for each applied load value.

3. Results

3.1. Deposition rate

Atomised spray deposition using perfluorotributylamine in the absence of plasma ignition resulted in negligible film growth rate (below 0.1 ± 0.1 nm min^{-1} following solvent washing of the deposited layer), thereby signifying the importance of plasma activation of the atomised droplets as well as the substrate surface for adhesion. The optimal atomised spray plasma deposition (ASPD) rate for the perfluorotributylamine precursor was measured to be 49 ± 4 nm min^{-1} at a liquid flow rate of 16 ± 4 × 10^{-4} mL s^{-1}. This value is an order of magnitude greater than that reported for conventional vapour phase perfluorotributylamine plasma deposition (5.9 nm min^{-1} growth rate [45])—which can be attributed to the higher precursor flow rate for atomised liquid droplets.

3.2. Contact angle

The wettability of the optimal deposition rate ASPD perfluorotributylamine layer (water contact angle = 114 ± 1°) was found to be comparable to its conventional vapour phase plasma deposited counterpart (water contact angle = 111° for coated flat substrate [46]), Fig. 2. A level of oleophobicity was also measured (hexadecane contact angle = 65 ± 1°) which is consistent with the reported hexadecane contact angle value of 68° for C8-perfluoroalkyl chain (perfluorooctyltrichlorosilane) self-assembled monolayers on flat silicon surfaces [47].

Incorporation of methacryloyl-SiO_2 nanoparticles into the ASPD perfluorotributylamine layer led to a significant enhancement in liquid repellency yielding water and hexadecane contact angles as high as 168 ± 5° and 90 ± 10° respectively for an optimal precursor slurry loading of 0.75% w/w silica nanoparticles, Fig. 2. For nanoparticle concentrations exceeding this loading, the nanoparticle slurry mixture became too viscous to sustain homogeneous atomisation. These liquid-repellent nanocoatings were stable towards washing with a 1:1 v/v propan-2-ol/cyclohexane polar/non-polar solvent mixture.

A variety of other nanoparticles were evaluated using this optimum nanoparticle concentration (0.75% w/w total). ASPD of perfluorotributylamine–(methacryloyl-SiO_2 + ZnO nanoparticles) significantly enhanced oil repellency further, achieving water and

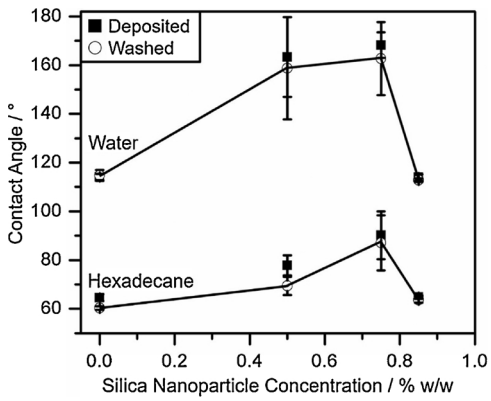

Fig. 2. Water and hexadecane contact angles for ASPD perfluorotributylamine–methacryloyl-SiO_2 nanocomposite coatings: as-deposited (■); and following rinsing with 1:1 v/v propan-2-ol/cyclohexane solvent mixture for 1 min (○). Uncoated glass substrate has water and hexadecane contact angles of 21 ± 3° and 8 ± 3° respectively.

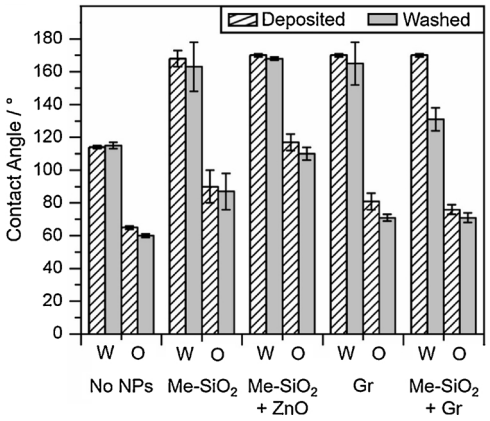

Fig. 3. Water (W) and hexadecane (O) contact angle values for ASPD perfluorotributylamine–nanoparticle composite layers: as-deposited, and rinsed with 1:1 v/v propan-2-ol/cyclohexane solvent mixture for 1 min. Using 0.75% w/w total nanoparticle slurry loading: methacryloyl-SiO_2 nanoparticles; methacryloyl-SiO_2 + ZnO nanoparticles (1:1 w/w); graphene; and methacryloyl-SiO_2 + graphene nanoparticles (1:1 w/w). The superhydrophobicity contact angle hysteresis values are reported in Table S 1.

hexadecane contact angle values of 168 ± 1° and 110 ± 4°, respectively, Fig. 3. These ASPD nanocomposite layers were stable towards polar/non-polar solvent rinsing. ASPD perfluorotributylamine–graphene layers displayed water contact angle values of 170 ± 1°, and 165 ± 13° for as-deposited and solvent-rinsed layers respectively. In the case of ASPD perfluorotributylamine–(methacryloyl-SiO_2 + graphene) nanocomposite layers, the water contact angle dropped from 170° to ~130° following solvent rinsing—this can be attributed to some low molecular weight species being present on the surface, Fig. 3. Overall, the ASPD perfluorotributylamine–(methacryloyl-SiO_2 + ZnO) nanocomposite layers displayed the highest liquid repellency towards water and oil (hexadecane).

3.3. X-ray photoelectron spectroscopy

XPS analysis of the ASPD perfluorotributylamine layer detected the presence of only carbon, fluorine, and nitrogen, Table 1. The absence of any Si(2p) and O(1s) XPS signals confirmed pin-hole free coverage of the deposited layer over the underlying silicon substrate. For the case of ASPD perfluorotributylamine–methacryloyl-SiO_2 nanocomposite and perfluorotributylamine–(methacryloyl-SiO_2 + ZnO) nanocomposite layers, less than 0.2 at.% of silicon or zinc XPS signal, and a small amount of oxygen were detected, which confirms that the nanoparticles remain encapsulated within perfluorotributylamine–nanoparticle slurry droplets during atomised spray plasma deposition (0.2–5 nm XPS sampling depth [48]).

The C(1s) XPS spectra of ASPD perfluorotributylamine (and nanocomposite) layers were fitted to five Gaussian Mg $K\alpha_{1,2}$ components in conjunction with their corresponding Mg $K\alpha_3$ and Mg $K\alpha_4$ satellite peaks shifted towards lower binding energies by ~8.4 and ~10.2 eV respectively, Fig. 4 [49]. The C(1s) Mg $K\alpha_{1,2}$ components being: $-\underline{C}-CF_n$ at 286.1 eV, $-\underline{C}F-$ at 287.5 eV, $-\underline{C}F-CF_n$ at 289.2 eV, $-\underline{C}F_2-$ at 291.2 eV, and $-\underline{C}F_3$ at 293.1 eV [42,43,50]. Unsaturated and crosslinked carbon centres (defined as %[$-\underline{C}F-CF_n$] + %[$-\underline{C}F-$] + %[$-\underline{C}-CF_n$]) account for ~35% of the total atomic carbon composition in all of the ASPD perfluorotributylamine–nanocomposite layers (which is consistent with the measured decrease in F:C ratio compared to the precursor theoretical value), Table 1. There was no significant variability in the chemical composition or F:C ratio between the various ASPD perfluorotributylamine–nanocomposite layers, Supplementary Material Fig. S1.

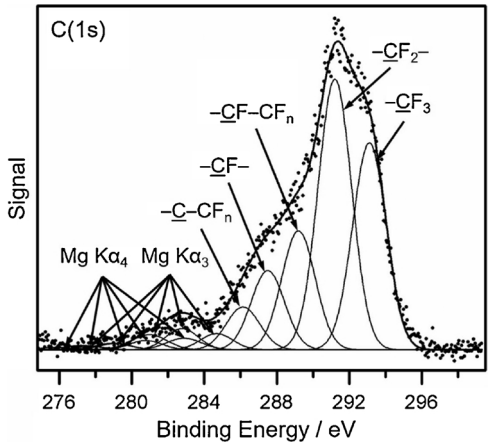

Fig. 4. C(1s) XPS spectrum of ASPD perfluorotributylamine layer. Mg $K\alpha_3$ and Mg $K\alpha_4$ satellite components are also shown [51].

The single N(1s) and F(1s) Mg $K\alpha_{1,2}$ peaks measured at 400.8 eV and 687.9 eV correspond to covalently bonded nitrogen and fluorine atoms respectively [50,52], Supplementary Material Fig. S2.

3.4. Infrared spectroscopy

The infrared spectrum obtained for the ASPD perfluorotributylamine layer displayed a broad band comprising perfluorinated chain $-CF_2-CF_3$ (1365–1325 cm^{-1}), $-CF_3$ (1350–1120 cm^{-1}), and $-CF_2-$ (1280–1120 cm^{-1}) absorbances, as well as $-C-N$ (1250–1020 cm^{-1}), Fig. 5 and Table 2 [46,57]. The observed shift of this broad peak (1365–1120 cm^{-1}) towards higher wavenumber with respect to the perfluorotributylamine precursor can be attributed to defluorination and crosslinking of the perfluoroalkyl chains during plasma-assisted deposition [53]—which is consistent with the decrease of F:C XPS ratio measured for the ASPD perfluorotributylamine layer, Table 1. The band at 1731 cm^{-1} can be attributed to $-CF{=}CF-$ stretching (not carbonyl stretching given the absence of any oxygen detected by XPS, Table 1 [54]) [45,55].

Overall, it is evident that there is nanoparticle incorporation within the bulk of all the ASPD perfluorotributylamine nanocomposite layers (sampling depth of 0.5–20 μm for RAIRS [61]). Infrared spectra of methacryloyl-SiO_2 nanoparticles display a band shoulder in the 1100–1000 cm^{-1} region associated with $Si-O-Si$ stretching [62,63].

Table 1
XPS compositions for precursor (theoretical) and ASPD perfluorotributylamine–nanoparticle layers.

System	Atomic Composition / %						F:C ratio	C(1s) Component / %				
	C	F	N	O	Si	Zn		$-\underline{C}-CF_n$	$-\underline{C}F-$	$-\underline{C}F-CF_n$	$-\underline{C}F_2-$	$-\underline{C}F_3$
Theoretical	30	67.5	2.5	–	–	–	2.25	–	–	–	75	25
No Nanoparticle	34.9 ± 0.2	58.2 ± 0.0	6.9 ± 0.2	0.0 ± 0.0	–	–	1.7 ± 0.0	7.3 ± 1.8	11.0 ± 0.0	16.7 ± 0.2	36.9 ± 1.1	28.1 ± 0.9
SiO_2	33.8 ± 0.1	58.5 ± 0.3	6.9 ± 0.1	0.6 ± 0.1	0.1 ± 0.2	–	1.7 ± 0.1	7.6 ± 0.4	13.4 ± 0.1	14.9 ± 0.5	35.9 ± 1.6	28.2 ± 1.4
SiO_2 + ZnO	34.4 ± 0.2	57.1 ± 0.3	7.1 ± 0.1	1.2 ± 0.4	0.0 ± 0.0	0.2 ± 0.0	1.7 ± 0.0	8.4 ± 1.0	11.1 ± 1.1	15.0 ± 0.8	37.1 ± 2.7	28.3 ± 1.5

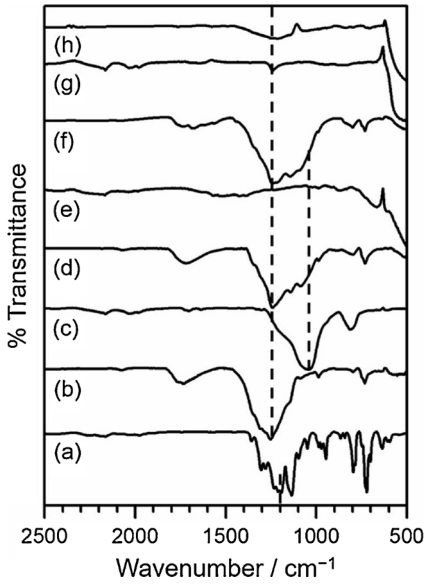

Fig. 5. Infrared spectra: (a) ATR perfluorotributylamine precursor; (b) RAIRS ASPD perfluorotributylamine layer; (c) ATR methacryloyl-SiO_2 nanoparticles; (d) RAIRS ASPD perfluorotributylamine–methacryloyl-SiO_2 nanocomposite layer (0.75% w/w nanoparticle concentration); (e) ATR ZnO nanoparticles; (f) RAIRS ASPD perfluorotributylamine–(methacryloyl-SiO_2 + ZnO) nanocomposite layer (0.75% w/w total nanoparticle concentration); (g) ATR graphene nanoplatelets; and (h) RAIRS ASPD perfluorotributylamine–graphene nanocomposite layer (0.75% w/w graphene concentration). Dashed lines correspond to perfluorinated chain (1365–1120 cm^{-1}), and Si—O—Si (1049 cm^{-1}) absorbances. The weak features in the 2160–2030 cm^{-1} range originate from the diamond substrate in the ATR cell [56].

Table 2
Infrared assignments for perfluorotributylamine precursor and ASPD nanocomposite layers [57–60].

Absorption Frequency/cm^{-1}	Assignment
1731	—CF=CF— stretching
1365–1325	$-CF_2-CF_3$ stretching
1350–1120	$-CF_3$ antisymmetric stretching
1280–1120	$-CF_2-$ stretching
1250–1020	C—N antisymmetric stretching
1100–1000	Si—O—Si stretching
1100–900	C—F stretching
980	$-CF_3$ symmetric stretching
815	Si—O—Si bending
605–505	Zn—O stretching

The presence of this feature confirmed incorporation of methacryloyl-SiO_2 nanoparticles into the ASPD perfluorotributylamine nanocomposite layers [64,65].

ZnO nanoparticles exhibit a strong infrared band at 605–505 cm^{-1} assigned to the stretching mode of Zn—O [60]. This was also observed for the ASPD perfluorotributylamine–(methacryloyl-SiO_2 + ZnO) nanocomposite layer in combination with the aforementioned methacryloyl-SiO_2 nanoparticle band shoulder feature at 1100–1000 cm^{-1}.

The ASPD perfluorotributylamine–graphene nanocomposite layer displayed a strong characteristic graphene infrared absorbance feature in the 600–450 cm^{-1} region.

3.5. Scanning electron microscopy

Scanning electron microscopy (SEM) images of ASPD perfluorotributylamine layers showed a flat surface morphology indicating the deposition of a smooth nanocoating, Fig. 6.

Incorporation of the various types of nanoparticles gave rise to hierarchical topographical structures. ASPD perfluorotributylamine–methacryloyl-SiO_2 nanocomposite layers present dispersed 3-level hierarchical roughness islands comprising a background nanoscale roughness superimposed onto microscale spherical asperities and larger cavities (ca. 12 µm diameter)—which correlate to the enhancement in water and hexadecane contact angle values, Fig. 2. A mixture of methacryloyl-SiO_2 and ZnO nanoparticles in the ASPD nanocomposite layers also resulted in hierarchical roughness but yielded a more evenly distributed hierarchical surface structure (no large-scale cavities which manifests in higher hexadecane contact angle values)—this may arise due to a better dispersed perfluorotributylamine/(methacryloyl-SiO_2 + ZnO) nanoparticle slurry mixture through the use of trifluoroacetic acid fluorosurfactant, Fig. 3. Such hierarchical roughness lowers liquid–solid interaction due to air pockets in accordance with the Cassie–Baxter model for surface wetting [14].

ASPD nanocomposite layers containing graphene lacked significant nanoscale structure and presented a more globular microscale roughness (presumably due to the larger platelet size of graphene), and consequently displays the lowest hexadecane contact angle values amongst the range of ASPD nanocomposite layers, Fig. 3.

3.6. Microindentation

Microindentation measurements showed nanoparticle incorporation significantly improves the hardness of ASPD nanocomposite layers. Also, they displayed indentation-resistance at applied loads below 245 mN, Fig. 7. In all cases, the hardness improved by at least two-fold. Microindentation Vickers hardness of the ASPD perfluorotributylamine–(methacryloyl-SiO_2 + ZnO) nanocomposite layers was found to be as hard as the layers containing just methacryloyl functionalised SiO_2 nanoparticles. ASPD perfluorotributylamine–graphene nanocomposite layers further enhanced the hardness value (10.7 ± 0.8 GPa at an applied force of 980 mN). ASPD perfluorotributylamine–(methacryloyl-SiO_2 + graphene) nanocomposite layers presented the highest hardness values.

4. Discussion

Atomised spray plasma deposition (ASPD) is a solventless, single-step, and substrate-independent method for the deposition of functional nanocoatings [66–71]. Nanoparticles mixed with a fluorocarbon precursor to form a slurry mixture have been atomised into an electrical discharge and directed towards a target substrate. Plasma-excited species (mainly electrons, ions, and radicals) activate precursor–nanoparticle slurry droplets during impact onto the plasma-activated substrate leading to nanocomposite film growth.

Perfluorocarbon groups display weak intermolecular interactions due to the high electronegativity and electron-withdrawing effect of fluorine atoms. Hence, long perfluorocarbon chain lengths are able to lower the surface energy because of such weak intermolecular forces, thereby enhancing liquid repellency [72]. This accounts for the hydrophobic contact angle measured for the ASPD perfluorotributylamine layer containing no nanoparticles, where a lack of surface roughness is likely to make the Cassie-Baxter effect insignificant, Figs. 3 and 6. The XPS elemental composition N:C:F ratio of 1.0:5.1:8.4 for the ASPD perfluorotributylamine layer can be correlated to the characteristic low energy electron-impact fragmentation molecular ion formed from perfluorotributylamine in the gas phase: $C_5F_{10}N^+$ (m/z of 264) with a molecular structure of $CF_3CF_2CF_2CF{=}N^+{=}CF_2$ (N:C:F ratio of 1:5:10), Table 1, and Supplementary Material Table S2 [73,74]. This is consistent with the high level of nitrogen atom incorporation measured by XPS (6.9 at.% compared to the precursor theoretical value of 2.5 at.%, Table 1). The associated unsaturation and crosslinking in the deposited layer gives rise to a hard polymeric nanocoating, Fig. 7.

Further enhancement in liquid repellency has been achieved

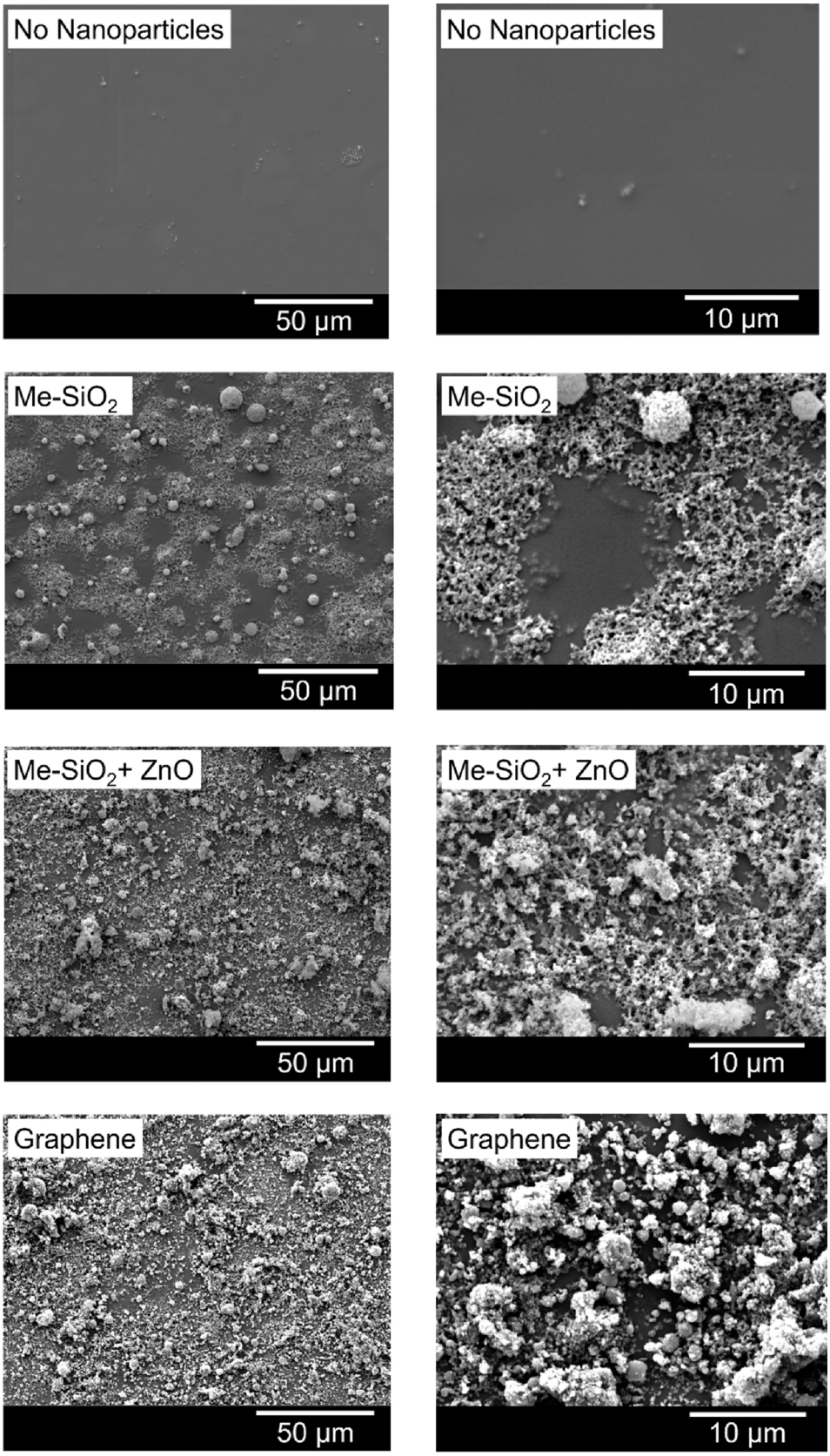

Fig. 6. SEM images of ASPD perfluorotributylamine nanocomposite layers containing different types of nanoparticles.

through the introduction of micro-/nanoscale hierarchical roughness by incorporating nanoparticles to generate a composite layer in accordance with the Cassie–Baxter model [14] and the lotus leaf effect [13]. This inclusion of different sized nanoparticles within the perfluorocarbon plasma polymer host matrix improves liquid repellency as well as the nanocomposite film mechanical properties, Figs. 3 and 7. By

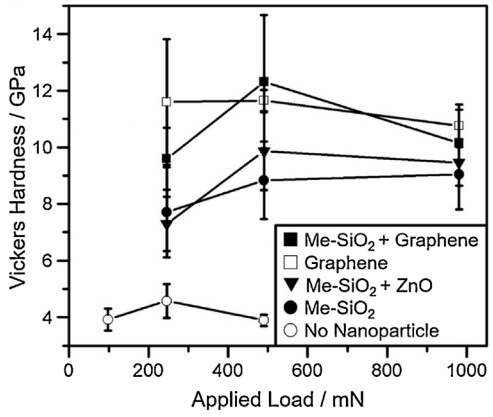

Fig. 7. Microindentation Vickers hardness as a function of applied loads for ASPD nanocomposite layers (0.75% w/w total nanoparticle concentration) for: (methacryloyl-SiO_2 + graphene), graphene, (methacryloyl-SiO_2 + ZnO), and methacryloyl-SiO_2 nanoparticle slurry mixtures. Microindentation below 245 mN load for the nanocomposite coatings resulted in no visible indentation (indentation-resistance). The Vickers hardness of reference 316 stainless steel was measured to be 1.9 ± 0.3 GPa.

utilising reactive (methacryloyl) functionalised silica nanoparticles, greater bonding is promoted within the growing fluorocarbon polymer matrix via plasma excitation. For comparable applied loads (980 mN), the ASPD perfluorotributylamine–graphene nanocomposite layer displays hardness values exceeding stainless steel (10.7 GPa versus 1–2 GPa respectively) [75].

5. Conclusions

Atomisation of fluorocarbon precursor–nanoparticle slurries into a low temperature non-equilibrium electrical discharge leads to the deposition of nanocomposite layers. For the case of perfluorotributylamine based slurries containing methacryloyl functionalised silica, zinc oxide, or graphene nanoparticles, it has been found that low surface energy hierarchical roughness nanocoatings are deposited which display enhanced levels of repellency towards water and oil liquids. There is also a significant improvement in mechanical properties yielding an order of magnitude greater hardness compared to stainless steel.

Conflicts of interest

There are no conflicts of interest to declare.

Author contributions

J. P. S. B. and I. C.-M. devised the bioinspired approach for superhydrophobic nanocomposite surfaces. I. C.-M. performed atomised spray plasma deposition. A. W. R. and I. C.-M. performed XPS. The manuscript was jointly drafted by J. P. S. B. and I. C.-M. All authors gave final approval for publication.

Data accessibility

Supporting data can be accessed at http://collections.durham.ac.uk.

Acknowledgements

This work was supported by Engineering and Physical Sciences Research Council (EPSRC) grant reference EP/J005401/1 and PhD studentship (reference EP/M507854/1) for A. W. Ritchie. I. Castaneda-Montes thanks Mexico CONACyT for scholarship reference 409139. Dr. J. J. Wu is thanked for providing access to the Vickers hardness instrumentation.

Appendix A. Supplementary data

Supplementary material related to this article can be found, in the online version, at doi:https://doi.org/10.1016/j.colsurfa.2018.08.054.

References

[1] Y. Liu, Q. Wang, X. Zhu, F. Yang, M.Y. Akram, J. Nie, Preparation of superhydrophobic surface via one-step photopolymerization, Mater. Lett. 190 (2017) 48–51.
[2] F. Chu, X. Wu, L. Wang, Meltwater evolution during defrosting on superhydrophobic surfaces, ACS Appl. Mater. Interfaces 10 (2018) 1415–1421.
[3] F.J.M. Ruiz-Cabello, P.F. Ibáñez-Ibáñez, J.F. Gómez-Lopera, J. Martínez-Aroza, M. Cabrerizo-Vílchez, M.A. Rodríguez-Valverde, Testing the performance of superhydrophobic aluminum surfaces, J. Colloid Interfaces Sci. 508 (2017) 129–136.
[4] U. Zulfiqar, M. Awais, S.Z. Hussain, I. Hussain, S.W. Husain, T. Subhani, Durable and self-healing superhydrophobic surfaces for building materials, Mater. Lett. 192 (2017) 56–59.
[5] B. Li, X. Wang, H.Y. Jung, Y.L. Kim, J.T. Robinson, M. Zalalutdinov, S. Hong, J. Hao, P.M. Ajayan, K.-T. Wan, Y.-J. Jung, Printing highly controlled suspended carbon nanotube network on micro-patterned superhydrophobic flexible surface, Sci. Rep. 5 (2015) 1–9.
[6] H. Li, S. Yu, A robust superhydrophobic surface and origins of its self-cleaning properties, Appl. Surf. Sci. 420 (2017) 336–345.
[7] H. Qian, M. Li, Z. Li, Y. Lou, L. Huang, D. Zhang, D. Xu, C. Du, L. Lu, J. Gao, Mussel-inspired superhydrophobic surfaces with enhanced corrosion resistance and dual-action antibacterial properties, Mater. Sci. Eng. 80 (2017) 566–577.
[8] M. Werb, C.F. García, N.C. Bach, S. Grumbein, S.A. Sieber, M. Opitz, O. Lieleg, Surface topology affects wetting behavior of *Bacillus subtilis* biofilms, NPJ Biofilms Microbiomes 3 (2017) 1–11.
[9] M. Cheng, S. Zhang, H. Dong, S. Han, H. Wei, F. Shi, Improving the durability of a drag-reducing nanocoating by enhancing its mechanical stability, ACS Appl. Mater. Interfaces 7 (2015) 4275–4282.
[10] X. Su, H. Li, X. Lai, L. Zhang, T. Liang, Y. Feng, X. Zeng, Polydimethylsiloxane-based superhydrophobic surfaces on steel substrate: fabrication, reversibly extreme wettability and oil–water separation, ACS Appl. Mater. Interfaces 9 (2017) 3131–3141.
[11] P.S. Brown, O.D.L.A. Atkinson, J.P.S. Badyal, Ultrafast oleophobic–hydrophilic switching surfaces for antifogging, self-cleaning, and oil–water separation, ACS Appl. Mater. Interfaces 6 (2014) 7504–7511.
[12] S. Hoshian, E. Kankuri, R.H.A. Ras, S. Franssila, V. Jokinen, Water and blood repellent flexible tubes, Sci. Rep. 7 (2017) 1–8.
[13] W. Barthlott, C. Neinhuis, Purity of the sacred lotus, or escape from contamination in biological surfaces, Planta 202 (1997) 1–8.
[14] A.B.D. Cassie, S. Baxter, Wettability of porous surfaces, Trans. Faraday Soc. 40 (1944) 546–551.
[15] A. Steele, I. Bayer, E. Loth, Inherently superoleophobic nanocomposite coatings by spray atomization, Nano Lett. 9 (2009) 501–505.
[16] Q. Liu, D. Chen, Z. Kang, One-step electrodeposition process to fabricate corrosion-resistant superhydrophobic surface on magnesium alloy, ACS Appl. Mater. Interfaces 7 (2015) 1859–1867.
[17] N. Yokoi, K. Manabe, M. Tenjimbayashi, S. Shiratori, Optically transparent superhydrophobic surfaces with enhanced mechanical abrasion resistance enabled by mesh structure, ACS Appl. Mater. Interfaces 7 (2015) 4809–4816.
[18] W. Chen, A.Y. Fadeev, M.C. Hsieh, D. Öner, J. Youngblood, T.J. McCarthy, Ultrahydrophobic and ultralyophobic surfaces: some comments and examples, Langmuir 15 (1999) 3395–3399.
[19] M. Järn, M. Heikkilä, M. Lindén, Bioinspired synthesis of superhydrophobic coatings, Langmuir 24 (2008) 10625–10628.
[20] F. Lapierre, Y. Coffinier, R. Boukherroub, V. Thomy, Electro-(de)wetting on superhydrophobic surfaces, Langmuir 29 (2013) 13346–13351.
[21] P.S. Brown, B. Bhushan, Mechanically durable, superomniphobic coatings prepared by layer-by-layer technique for self-cleaning and anti-smudge, J. Colloid Interfaces Sci. 456 (2015) 210–218.
[22] J.A. Syed, S. Tang, X. Meng, Super-hydrophobic multilayer coatings with layer number tuned swapping in surface wettability and redox catalytic anti-corrosion application, Sci. Rep. 7 (2017) 1–17.
[23] Y. Wang, Y. Shi, L. Pan, M. Yang, L. Peng, S. Zong, Y. Shi, G. Yu, Multifunctional superhydrophobic surfaces templated from innately microstructured hydrogel matrix, Nano Lett. 14 (2014) 4803–4809.
[24] D. Wu, S.-Z. Wu, Q.-D. Chen, Y.-L. Zhang, J. Yao, X. Yao, L.-G. Niu, J.-N. Wang, L. Jiang, H.-B. Sun, Curvature-driven reversible in situ switching between pinned and roll-down superhydrophobic states for water droplet transportation, Adv. Mater. 23 (2011) 545–549.
[25] P.S. Brown, E.L. Talbot, T.J. Wood, C.D. Bain, J.P.S. Badyal, Superhydrophobic hierarchical honeycomb surfaces, Langmuir 28 (2012) 13712–13719.
[26] J. Ryu, K. Kim, J. Park, B.G. Hwang, Y. Ko, H. Kim, J. Han, E. Seo, Y. Park, S.J. Lee, Nearly perfect durable superhydrophobic surfaces fabricated by a simple one-step plasma treatment, Sci. Rep. 7 (2017) 1–8.
[27] Y. Lu, S. Sathasivam, J. Song, C. Crick, C. Carmalt, I. Parkin, Robust self-cleaning surfaces that function when exposed to either air or oil, Science 347 (2015) 1132–1135.
[28] M. Abolghasemibizaki, R. Mohammadi, Droplet impact on superhydrophobic surfaces fully decorated with cylindrical macrotextures, J. Colloid Interfaces Sci. 509

(2018) 422–431.
[29] M.P. Bonnar, B.M. Burnside, J. Christie, E.J. Sceal, C.E. Troupe, J.I. Wilson, Hydrophobic coatings from plasma polymerized vinyltrimethylsilane, Chem. Vap. Depos. 5 (1999) 117–125.
[30] Y. Li, H. Shao, P. Lv, C. Tang, Z. He, Y. Zhou, M. Shuai, J. Mei, W.-M. Lau, Fast preparation of mechanically stable superhydrophobic surface by UV cross-linking of coating onto oxygen-inhibited layer of substrate, Chem. Eng. J. 338 (2018) 440–449.
[31] F. Fanelli, A. Mastrangelo, F. Fracassi, Aerosol-assisted atmospheric cold plasma deposition and characterization of superhydrophobic organic–inorganic nanocomposite thin films, Langmuir 30 (2014) 857–865.
[32] M. Sadej, H. Gojzewski, E. Andrzejewska, Photocurable polymethacrylate-silica nanocomposites: correlation between dispersion stability, curing kinetics, morphology and properties, J. Polym. Res. 23 (2016) 116–127.
[33] M. Buchholz, Q. Li, H. Noei, A. Nefedov, Y. Wang, M. Muhler, K. Fink, C. Wöll, The interaction of formic acid with zinc oxide: a combined experimental and theoretical study on single crystal and powder samples, Top. Catal. 58 (2015) 174–183.
[34] H. Chen, H. Muthuraman, P. Stokes, J. Zou, X. Liu, J. Wang, Q. Huo, S.I. Khondaker, L. Zhai, Dispersion of carbon nanotubes and polymer nanocomposite fabrication using trifluoroacetic acid as a co-solvent, Nanotechnology 18 (2007) 415606.
[35] C.D. Ehrlich, J.A. Basford, Recommended practices for the calibration and use of leaks, J. Vac. Sci. Technol. A 10 (1992) 1–17.
[36] H.L. Berger, D.F. Mowbray, R.A. Copeman, R.J Russell, Ultrasonic Atomizing Nozzle and Method. U.S. Patent US 7,712,680 B2, May 11, 2010.
[37] Sono-Tek, http://www.sono-tek.com/drop-size-and-distribution/ (Accessed 8 March 2018).
[38] R.E. Johnson Jr, R.H. Dettre, Wetting of low-energy surfaces, in: J.C. Berg (Ed.), Wettability, Marcel Dekker, Inc, New York, 1993Chapter 1, p 13.
[39] D. Briggs, XPS: basic principles, spectral features and qualitative analysis, in: D. Briggs, J.T. Grant (Eds.), Surface Analysis by Auger and X-Ray Photoelectron Spectroscopy, IM Publications and Surface Spectra Limited, England, 2003, pp. 52–54.
[40] R.M. Friedman, J. Hudis, M.L. Perlam, Chemical effects on linewidths observed in photoelectron spectroscopy, Phys. Rev. Lett. 29 (1972) 692–695.
[41] J.F. Evans, J.F. Gibson, J.H. Moulder, J.S. Hammond, H. Goretzki, Angle resolved ESCA analysis of plasma modified polystyrene, Fresenius J. Anal. Chem. 319 (1984) 841–844.
[42] D.T. Clark, D. Shuttleworth, Plasma polymerization. II. An ESCA investigation of polymers synthesized by excitation of inductively coupled RF plasma in perfluorobenzene and perfluorocyclohexane, J. Polym. Sci. Polym. Chem. Ed. 18 (1980) 27–46.
[43] A.M. Hynes, M.J. Shenton, J.P.S. Badyal, Pulsed plasma polymerization of perfluorocyclohexane, Macromolecules 29 (1996) 4220–4225.
[44] ASTM, ASTM Standard E 384–11e1, Standard Test Method for Knoop and Vickers Hardness of Materials, ASTM, International, West Conshohocken, PA, 2011.
[45] M.R. Yang, K.S. Chen, J.L. He, The interaction between blood and the surface characteristics of plasma polymerized films, Mater. Chem. Phys. 48 (1997) 71–75.
[46] F. Reniers, N. Vandencasteele, O. Bury, Method for Depositing a Fluorinated Layer from a Precursor Monomer. U.S. Patent US2011/0014395 A1, Jan 20, 2011.
[47] C. Aulin, S.H. Yun, L. Wagberg, T. Lindstrom, Design of highly oleophobic cellulose surfaces from structured silicon templates, ACS Appl. Mater. Interfaces 1 (2009) 2443–2452.
[48] D. Briggs, Surface Analysis of Polymers by XPS and Static SIMS, Cambridge University Press, 1998, pp. 34–39.
[49] S. Hofmann, Instrumentation, Auger- and X-Ray Photoelectron Spectroscopy in Materials Science. A User-Oriented Guide; Springer Series in Surface Science vol. 49, Springer-Verlag, Berlin, 2013, pp. 18–19.
[50] G. Beamson, D. Briggs, High-Resolution XPS of Organic Polymers. The Scienta ESCA300 Database, John Wiley and Sons, Chichester, England, 1992, p. 278.
[51] J.F. Moulder, W.F. Stickle, P.E. Sobol, K.D. Bomben, Data interpretation, Handbook of X-Ray Photoelectron Spectroscopy, Perkin-Elmer Corporation, Minnesota, USA, 1992 pp 18.
[52] D.T. Clark, The modification, degradation, and synthesis of polymer surfaces studied by ESCA, in: D.W. Dwight, T.J. Fabish, H.R. Thomas (Eds.), Photon, Electron, and Ion Probes of Polymer Structure and Properties, American Chemical Society, Washington, DC, 1981, pp. 247–291. ACS Symposium Series 162.
[53] S. Agraharam, D.W. Hess, P.A. Kohl, S.A. Bidstrup Allen, Plasma chemistry in fluorocarbon film deposition from pentafluoroethane/argon mixtures, J. Vac. Sci. Technol. A 17 (1999) 3265–3271.
[54] K.S. Chen, Y.N. Chang, J.L. Her, Surface characteristics and blood compatibility of plasma polymerized perfluorotributylamine films, ISPC-8 Tokyo, (1987), pp. 1340–1346.
[55] C.P. Lungu, A.M. Lungu, M. Akazawa, Y. Sakai, H. Sugawara, M. Tabata, Fluorinated carbon films with low dielectric constant made from novel fluorocarbon source materials by RF plasma enhanced chemical vapour deposition, Jpn. J. Appl. Phys. Part 2 38 (1999) L 1544–L 1546.
[56] K. Wada, Shimadzu Corporation. International Marketing Division, FTIR Talk Letter vol. 11, (2009), pp. 1–10.
[57] D. Lin-Vien, N.B. Colthup, W.G. Fateley, J.G. Grasselli, The Handbook of Infrared and Raman Characteristic Frequencies of Organic Molecules, Academic Press, Inc., San Diego, 1991.
[58] L.J. Bellamy, The Infra-Red Spectra of Complex Molecules vol. 2, Chapman and Hall Ltd, London, 1975.
[59] E. Pretsch, P. Buhlmann, M. Badertscher, Structure Determination of Organic Compounds: Tables of Spectral Data, Springer-Verlag, Berlin, 2009.
[60] M.I. Khalil, M.M. Al-Qunaibit, A.M. Al-zahem, J.P. Labis, Synthesis and characterization of ZnO nanoparticles by thermal decomposition of a curcumin zinc complex, Arab. J. Chem. 7 (2014) 1178–1184.
[61] C.L. Chakrabarti, G. Akh, J.C. Hutton, ATR and reflectance IR spectroscopy, applications, Spectrochim. Acta B 33 (1999) 153–193.
[62] D. Goswami, S.K. Medda, G. De, Superhydrophobic films on glass surface derived from trimethylsilanized silica gel nanoparticles, ACS Appl. Mater. Interfaces 3 (2011) 3440–3447.
[63] J.-K. Hong, H.-R. Kim, H.-H. Park, The effect of sol on the sol–gel derived low density SiO_2 xerogel film for intermetal dielectric application, Thin Solid Films 332 (1998) 449–454.
[64] Y. Li, J.A. Yerian, S.A. Khan, P.S. Fedkiw, Crosslinkable fumed silica-based nanocomposite electrolytes for rechargeable lithium batteries, J. Power Sources 161 (2006) 1288–1296.
[65] D.B. Stojanović, L. Brajović, A. Orlović, D. Dramlić, V. Radmilović, P.S. Uskoković, R. Aleksić, Transparent PMMA/silica nanocomposites containing silica nanoparticles coating under supercritical conditions, Prog. Org. Coat. 76 (2013) 626–631.
[66] L.J. Ward, W.C.E. Schofield, J.P.S. Badyal, Atmospheric pressure plasma deposition of structurally well-defined polyacrylic acid films, Chem. Mater. 15 (2003) 1466–1469.
[67] T.J. Wood, L.J. Ward, J.P.S. Badyal, Super-adhesive polymer-silica nanocomposite layers, ACS Appl. Mater. Interfaces 5 (2013) 9678–9683.
[68] T.J. Wood, P.S. Brown, J.P.S. Badyal, Atomized spray plasma deposition of structurally well-defined bioactive coatings, Plasma Chem. Plasma Process 34 (2014) 1019–1031.
[69] T.J. Wood, J.P.S. Badyal, Atomized spray plasma deposition (ASPD) of structurally well-defined alkyl functionalised layers, Surf. Coat. Technol. 227 (2013) 28–31.
[70] D. Vangeneugden, S. Paulussen, O. Goosens, R. Rego, K. Rose, Aerosol-assisted plasma deposition of barrier coatings using organic-inorganic sol-gel precursor systems, Chem. Vap. Depos. 11 (2005) 491–496.
[71] L.J. Ward, W.C.E. Schofield, J.P.S. Badyal, Atmospheric pressure glow discharge deposition of polysiloxane and SiO_x films, Langmuir 19 (2003) 2110–2114.
[72] S. Posner, Perfluorinated compounds: occurrence and uses in products, in: T.P. Knepper, F.T. Lange (Eds.), Polyfluorinated Chemicals and Transformation Products, Springer, Heidelberg, 2012, pp. 25–41.
[73] Perfluorotributylamine. National Institute of Standards and Technology. http://webbook.nist.gov/cgi/cbook.cgi?ID=C311897&Mask=200#Mass-Spec (Accessed 6 March 2018).
[74] M. Smith, Understanding Mass Spectra: A Basis Approach, John Wiley & Sons, Inc.: New Jersey, 2004, pp. 287–288.
[75] S. Qu, C.X. Huang, Y.L. Gao, G. Yang, S.D. Wu, Q.S. Zang, Z.F. Zhang, Tensile and compressive properties of AISI 304L stainless steel subjected to equal channel angular pressing, Mater. Sci. Eng. 475 (2008) 207–216.